Influence of Coronal Holes on CME Deflections: Numerical Study

Abril Sahade[1,2], Mariana Cécere[1,3] , and Gustavo Krause[4,5]

[1] Instituto de Astronomía Teórica y Experimental, CONICET-UNC, Córdoba, Argentina; asahade@unc.edu.ar
[2] Facultad de Matemática, Astronomía, Física y Computación, Universidad Nacional de Córdoba (UNC), Córdoba, Argentina
[3] Observatorio Astronómico de Córdoba, UNC, Córdoba, Argentina
[4] Instituto de Estudios Avanzados en Ingeniería y Tecnología (IDIT), CONICET, Córdoba, Argentina
[5] Facultad de Ciencias Exactas, Físicas y Naturales, UNC, Córdoba, Argentina

Abstract

The understanding of the causes that produce the deflection of coronal mass ejections (CMEs) is essential for the space weather forecast. We study the effects on CME trajectories produced by the different properties of a coronal hole (CH), close to the ejection area. We perform ideal magnetohydrodynamics simulations emulating the early rising of the CME in the presence of a CH. We find that, the stronger the magnetic field and the wider the CH area, the larger the CME deflection. The deflection reduces as the CH moves away from the ejection region. To quantify the deflection we propose a dimensionless parameter that depends on the CH properties. We show that a minimum magnetic energy region, responsible for the deflection, is associated with the presence of the CH near the CME. We establish a relationship between the CH properties, the location of the minimum magnetic region, and the CME deflection.

Unified Astronomy Thesaurus concepts: Solar physics (1476); Solar coronal holes (1484); Solar coronal mass ejections (310); Solar magnetic fields (1503); Space weather (2037); Magnetohydrodynamical simulations (1966); Magnetohydrodynamics (1964)

Supporting material: animation

1. Introduction

Coronal mass ejections (CMEs) are eruptive events in which large amounts of solar mass are released toward the interplanetary medium. They often interact with the Earth's magnetosphere and cause geomagnetic storms, making them objects of great interest for space weather forecasting studies. It is known that CMEs do not always evolve in a radial direction but can deviate due to multiple factors, complicating the prediction of Earth encounters (Zhuang et al. 2017). The analysis of the coronal environment during the early stages of the CME's evolution is of utmost importance to estimate a probable trajectory. The CMEs deviations from the radial direction (deflection, hereafter) are mainly attributed to the distribution of several magnetic structures surrounding the CME formation area, namely coronal holes (CHs; e.g., Cremades et al. 2006; Gopalswamy et al. 2009; Kilpua et al. 2009; Xie et al. 2009; Panasenco et al. 2013), active regions (ARs; e.g., Kay et al. 2015; Möstl et al. 2015), pseudostreamers (e.g., Lynch & Edmondson 2013), streamer belts (SBs; e.g., Zuccarello et al. 2012; Kay et al. 2013; Yang et al. 2018), and heliospheric current sheets (HCSs; e.g., Liewer et al. 2015; Wang et al. 2019).

Currently in the literature, the main coronal magnetic structures related with low magnetic energy regions are pseudostreamers (PSs), SBs, or HCSs. These structures act as potential wells where the CMEs are believed to "fall," changing their radial trajectory. On the other hand, the strong gradients of the magnetic field strength in the neighborhood of ARs are responsible for the CME deflection. Moreover, CHs seem to act as magnetic walls, because CMEs cannot penetrate their open magnetic field and are pushed in the opposite direction.

There are several case studies (see, e.g., Jin et al. 2017; Yang et al. 2018; Cécere et al. 2019), where the deflection of the analyzed CME seems to be produced by the interaction with a nearby CH. In these studies, the CMEs move away from the CH region. In studies of observational multievents, the influence of CHs in the CMEs trajectory is studied by means of a quantity that represents a fictitious force, which depends on both the area of the CH and its distance to the CME (Cremades et al. 2006). These studies show a good agreement between the measured deviation and the sum of all fictitious forces of the holes.

In addition, Gopalswamy et al. (2009) analyzed the influence of CHs in the evolution of six CMEs using an influence parameter, which includes the CH magnetic field strength. They concluded that open field lines of CHs act as magnetic walls that constrain the CME propagation. Also, the study of a large amount of magnetic clouds (MCs) and non-MCs, show that the deflection of interplanetary CMEs are influenced by CHs (Mäkelä et al. 2013).

Many efforts have been made to numerically understand the behavior of coronal mass ejections. Several works in the literature were devoted to study the capability of different magnetic structures nearby CME locations to produce a deflection (see, e.g., Lugaz et al. 2011; Zuccarello et al. 2012; Lynch & Edmondson 2013; Zhou et al. 2014). Other multicase MHD simulations (see, e.g., Zhou & Feng 2013) study magnetic structures containing regions of low magnetic energy, or imbalances in the magnetic pressure and tension, or imbalanced magnetic tension and pressure gradients and reconnections that result in magnetic forces driving the CME deviation.

A method to analyze how the trajectory of CMEs is altered is the ForeCAT model (Kay et al. 2013, 2015). Taking into account the CME properties (e.g., mass, expansion, velocity, etc.), it determines how the magnetic forces, produced by different background magnetic structures, affect the CME

radial trajectory. Using this model, Capannolo et al. (2017) analyzed the deviation of the CME event of 2008 April 9 and suggested that the prominence dynamic itself causes the CME deviation.

In most observations the CME deflections are detected at coronagraph altitudes ($>1.5\,R_\odot$), with few cases at larger altitudes than $1.12\,R_\odot$ (see, e.g., Landi et al. 2010; Panasenco et al. 2011; Zuccarello et al. 2012; Panasenco et al. 2013; Capannolo et al. 2017). To study the deflection occurrences, it is necessary to characterize the coronal environment during the first evolution ejection stages, at low coronal levels (until $1.5\,R_\odot$). Due to the complexity of the magnetic environment surrounding the CME, it is difficult to quantify the action of each magnetic structure on the CME trajectory.

In the present work we numerically study the effect of CHs in an isolated CME flux rope with the aim of characterizing its deflection as a function of the CH features and the magnetic environment configuration. To model the CME evolution in different magnetic scenarios with the presence of a CH, we carry out numerical simulations of the ideal MHD equations in 2.5 dimensions. This allows us to analyze the effect of each property of the CH (area, distance, and magnetic field strength) in the early stages of the CME evolution. We think that this systematic study contributes to the understanding of the CME behavior and its interaction with CHs.

2. The Model

The basic model starts with the ideal MHD equations in the presence of a gravitational field, which arise from considering the macroscopic behavior of a compressible ideal fully ionized plasma. The ideal MHD equations for a Cartesian system in its conservative form and in CGS units are written as:

$$\frac{\partial \rho}{\partial t} + \boldsymbol{\nabla} \cdot (\rho \boldsymbol{v}) = 0, \tag{1}$$

$$\frac{\partial (\rho \boldsymbol{v})}{\partial t} + \boldsymbol{\nabla} \cdot \left(\rho \boldsymbol{v}\boldsymbol{v} - \frac{1}{4\pi}\boldsymbol{B}\boldsymbol{B} \right) + \boldsymbol{\nabla} p + \frac{1}{8\pi}\boldsymbol{\nabla} B^2 = \rho \boldsymbol{g}, \tag{2}$$

$$\frac{\partial E}{\partial t} + \boldsymbol{\nabla} \cdot \left[\left(E + p + \frac{B^2}{8\pi} \right)\boldsymbol{v} - \frac{1}{4\pi}(\boldsymbol{v} \cdot \boldsymbol{B})\boldsymbol{B} \right] = \rho \boldsymbol{g}\boldsymbol{v}, \tag{3}$$

$$\frac{\partial \boldsymbol{B}}{\partial t} + \boldsymbol{\nabla} \cdot (\boldsymbol{v}\boldsymbol{B} - \boldsymbol{B}\boldsymbol{v}) = \boldsymbol{0}, \tag{4}$$

where ρ indicates the plasma density, p the thermal pressure, $\boldsymbol{v}$ the velocity, $\boldsymbol{B}$ the magnetic field, $\boldsymbol{g}$ the gravity acceleration, and E the total energy (per unit volume) given by

$$E = \rho\epsilon + \frac{1}{2}\rho v^2 + \frac{B^2}{8\pi},$$

where ϵ is the internal energy and

$$\boldsymbol{j} = \frac{c}{4\pi}\boldsymbol{\nabla} \times \boldsymbol{B},$$

is the current density, with c the speed of light.

In addition to the MHD equations, the divergence-free condition of the magnetic field, i.e.,

$$\boldsymbol{\nabla} \cdot \boldsymbol{B} = 0, \tag{5}$$

must be fulfilled.

To complete the set of MHD equations a closure relation among the thermodynamic variables must be imposed. We assume a calorically perfect gas for which $p = 2\rho k_B T / m_i = (\gamma - 1)\rho\epsilon$, where k_B is the Boltzmann constant, T the

plasma temperature, m_i the proton mass (assuming that the plasma is fully ionized hydrogen), and $\gamma = 5/3$ the specific heat relation.

2.1. Numerical Code

In order to evaluate the plasma behavior, the MHD Equations (1)–(4) are numerically solved in a two-dimensional Cartesian grid of colocated finite volumes. We perform 2.5D simulations to consider the z-direction magnetic field component in the interior of the flux rope, which are carried out using the FLASH Code (Fryxell et al. 2000), an open-source publicly available suite of high-performance simulation tools developed at the Center for Astrophysical Thermonuclear Flashes (Flash Center) of the University of Chicago. This code, currently in its fourth version, uses the finite volume method with Godunov-type schemes to solve the high energy compressible MHD equations on regular grids with adaptive mesh refinement (AMR) capabilities. For our simulations we choose the USM (unsplit staggered mesh) solver available in FLASH, for which it uses a second-order directionally unsplit scheme with a MUSCL-type reconstruction. This solver implements a more consistent treatment of the magnetic field, since its formulation is based on the constrained transport method and the corner transport upwind method, which avoids the generation of nonphysical magnetic field divergence (Lee & Deane 2009). To solve the interface Riemann problems we set the Roe's solver among the available options.

Cartesian 2D rectangular grids are used to represent the physical domain of $[-1000, 1000]$ Mm $\times$ $[0, 1000]$ Mm with an initial 80×40 discretization and nine refinement levels that take into account the pressure and temperature gradients. With this discretization we obtained a resolution of $\sim[0.1 \times 0.1]$ Mm^2 for the maximum refinement. Boundary conditions are set as follows. At both lateral ends outflow conditions (zero-gradient) are applied for the thermodynamic variables and the velocity to allow waves to leave the domain without reflection. The boundary conditions of the magnetic field at lateral ends require to extrapolate the initial force-free configuration to ghost cells in order to avoid the generation of spurious magnetic forces produced when assuming a zero-gradient evolution extrapolation in a nonconstant magnetic field. Obviously, this model is valid as long as shocks or disturbances do not reach the lateral ends of the domain. In the lower and the upper limits the hydrostatic boundary conditions must be imposed due to the effect of gravity, which acts in the y-direction and produces spurious fluxes through the top and the bottom of the domain if pressure and density are not correctly extrapolated. Therefore, to guarantee the conservation of the hydrostatic equilibrium at both ends we use the extrapolation proposed by Krause (2019) considering constant temperature through the boundary. The remaining variables (velocity and magnetic field components) at the upper boundary are extrapolated with a zero-gradient assumption, while for the lower boundary we impose the condition described by Robertson & Priest (1987) to ensure the line-tied magnetic field condition that is present in the solar surface during the CME evolution.

In addition to the described features of the numerical model, a particular treatment is required to correctly simulate the strong stratification of the background atmosphere. Then, to avoid spurious vertical velocities associated to the unbalance between the numerical fluxes and the discrete gravitational

source term when standard MUSCL-type schemes are used in strongly stratified atmospheres, we implement the local hydrostatic reconstruction scheme proposed by Krause (2019) to improve the preservation of hydrostatic equilibrium during the simulation.

Regarding the diffusive effects, we already established that the ideal MHD equations are used; therefore, there is no physical diffusion added to our experiments. Analytically, the ideal MHD model does not permit the magnetic reconnection, and thus a current sheet should be formed in the region below the flux rope where the magnetic lines are strongly stretched, which eventually causes the stopping of the flux rope rising (Forbes 1990). However, the numerical diffusion present in the simulations provides the necessary dissipation to prevent the current sheet formation allowing the ejection. We performed this analysis in a previous paper (Krause et al. 2018) where it is shown that the presence of anomalous magnetic resistivity in the region of the current sheet formation does not change the ejection velocity of the flux rope with respect to the ideal model. In this way, we can neglect the magnetic resistivity and use the ideal MHD equations, which allows a significant reduction in the computational cost.

2.2. Stratified Atmosphere

To simulate the solar atmosphere we adopt a multilayer atmosphere structure (Mei et al. 2012). The chromosphere is located between $y = 0$ and $y = h_{\rm ch}$ with constant temperature $T_{\rm ch}$. Above this, the transition region is extended to the base of the corona ($y = h_{\rm c}$), where the temperature grows linearly until $T_{\rm c}$, the constant temperature of the corona. Then the initial temperature distribution is given by

$$T(y) = \begin{cases} T_{\rm ch} & \text{if } 0 \leqslant y < h_{\rm ch} \\ (T_{\rm c} - T_{\rm ch})\left[\dfrac{y - h_{\rm ch}}{h_{\rm c} - h_{\rm ch}}\right] + T_{\rm ch} & \text{if } h_{\rm ch} \leqslant y < h_{\rm c} \\ T_{\rm c} & \text{if } h_{\rm c} \leqslant y. \end{cases} \quad (6)$$

We set up a temperature of $T_{\rm ch} = 10{,}000$ K at the chromosphere and $T_{\rm c} = 10^6$ K at the corona. The height of the chromosphere is $h_{\rm ch} = 10$ Mm; the transition region extends for 5 Mm until $h_{\rm c} = 15$ Mm, the base of the corona.

Considering the atmosphere is in hydrostatic equilibrium and current free, the pressure is obtained from the combination of the equation of state and Equation (2) with $\mathbf{v} = 0$. Then, taking a system with the y-axis aligned to the gravity acceleration but in the opposite direction (i.e., $\mathbf{g} = (0, -GM_\odot/(y + R_\odot)^2, 0)$, where G is the gravitational constant, $M_\odot$ is the Sun's mass, $R_\odot$ is the solar radius, and $y = 0$ corresponds to the solar surface), the hydrostatic pressure distribution is only a function of y:

$$p(y) = \begin{cases} p_{\rm ch} \exp\left[\left(\dfrac{h_{\rm ch}}{1 + h_{\rm ch}/R_\odot} - \dfrac{y}{1 + y/R_\odot}\right)\dfrac{\alpha}{T_{\rm ch}}\right] & \text{if } 0 \leqslant y < h_{\rm ch} \\ p_{\rm ch} \exp\left[-\displaystyle\int_{h_{\rm ch}}^{y} \dfrac{\alpha}{T(y')}\left(1 + \dfrac{y'}{R_\odot}\right)^{-2} dy'\right] & \text{if } h_{\rm ch} \leqslant y < h_{\rm c}, \\ p_{\rm c} \exp\left[-\dfrac{(y - h_{\rm c})}{1 + (y - h_{\rm c})/R_\odot}\dfrac{\alpha}{T_{\rm c}}\right] & \text{if } h_{\rm c} \leqslant y \end{cases}$$

where

$$p_{\rm ch}(y) = p_{\rm c} \exp\left[\int_{h_{\rm ch}}^{h_{\rm c}} \dfrac{\alpha}{T(y')}\left(1 + \dfrac{y'}{R_\odot}\right)^{-2} dy'\right],$$

and $\alpha = m_i g_\odot / 2k_B$, with $g_\odot = GM_\odot/R_\odot^2$.

The associated density is obtained from the equation of state, i.e.:

$$\rho = \frac{m_i p(y)}{2k_B T(y)}. \quad (7)$$

2.3. CME Model

The catastrophe model by Forbes (1990) consists of a magnetic configuration out of equilibrium driving the ejection of the flux rope (FR hereafter). Forbes proposed that the magnetic field of the FR is produced by a current wire (originally proposed by van Tend & Kuperus 1978). An image current wire is located below the photosphere in the opposite direction to generate a repulsive force. Also, the model includes a line dipole below the photosphere that provides an attractive force to the CME's wire and emulates the photospheric field. Figure 1(a) shows a scheme of the magnetic field (black dashed lines) of a flux rope (orange thick line) and a CH (violet region). In Figure 1(b) a current wire (the FR or the image current wire) is schematized, where we can describe three zones (Mei et al. 2012):

Z1: inside a current wire, $0 \leqslant R < r - \frac{\Delta}{2}$,

Z2: throughout the transition layer, $r - \frac{\Delta}{2} \leqslant R < r + \frac{\Delta}{2}$, and

Z3: outside a current wire, $r + \frac{\Delta}{2} \leqslant R$,

where r is the current wire radius, Δ is the thickness of the transition layer between the current wire and the exterior, and R is the radial coordinate from the center of the current wire.

The magnetic field component B_ϕ generated by a current wire with current distribution j_z, which are given by Equations (8) and (9):

$$B_\phi(R) = \begin{cases} \dfrac{2\pi}{c} j_0 R & \text{at Z1} \\ \dfrac{2\pi j_0}{cR}\left\{\dfrac{1}{2}\left(r - \dfrac{\Delta}{2}\right)^2 - \left(\dfrac{\Delta}{2}\right)^2 + \right. \\ \left. \dfrac{R^2}{2} + \dfrac{\Delta R}{\pi}\sin\left[\dfrac{\pi}{\Delta}\left(R - r + \dfrac{\Delta}{2}\right)\right] + \right. \\ \left. \left(\dfrac{\Delta}{\pi}\right)^2 \cos\left[\dfrac{\pi}{\Delta}\left(R - r + \dfrac{\Delta}{2}\right)\right]\right\} & \text{at Z2} \\ \dfrac{2\pi j_0}{cR}\left[r^2 + \left(\dfrac{\Delta}{2}\right)^2 - 2\left(\dfrac{\Delta}{\pi}\right)^2\right] & \text{at Z3,} \end{cases} \quad (8)$$

$$j_z(R) = \begin{cases} j_0 & \text{at Z1} \\ \dfrac{j_0}{2}\left\{\cos\left[\dfrac{\pi}{\Delta}\left(R - r + \dfrac{\Delta}{2}\right)\right] + 1\right\} & \text{at Z2} \\ 0 & \text{at Z3;} \end{cases} \quad (9)$$

where j_0 is a current density.

In order to obtain a helical magnetic field in the FR, to achieve densities and temperatures consistent with observational data of flux ropes, we include in the catastrophe model a magnetic field in z-axis of strength B_z. In this way, we avoid excessive gas pressure values needed to balance the magnetic pressure inside the flux rope in the initial equilibrium state. The component B_z of the magnetic field, and the current distribution j_ϕ, are described by:

$$B_z(R) = \frac{\sqrt{8}\,\pi j_1}{c}\sqrt{\left(r - \dfrac{\Delta}{2}\right)^2 - R^2}, \quad (10)$$
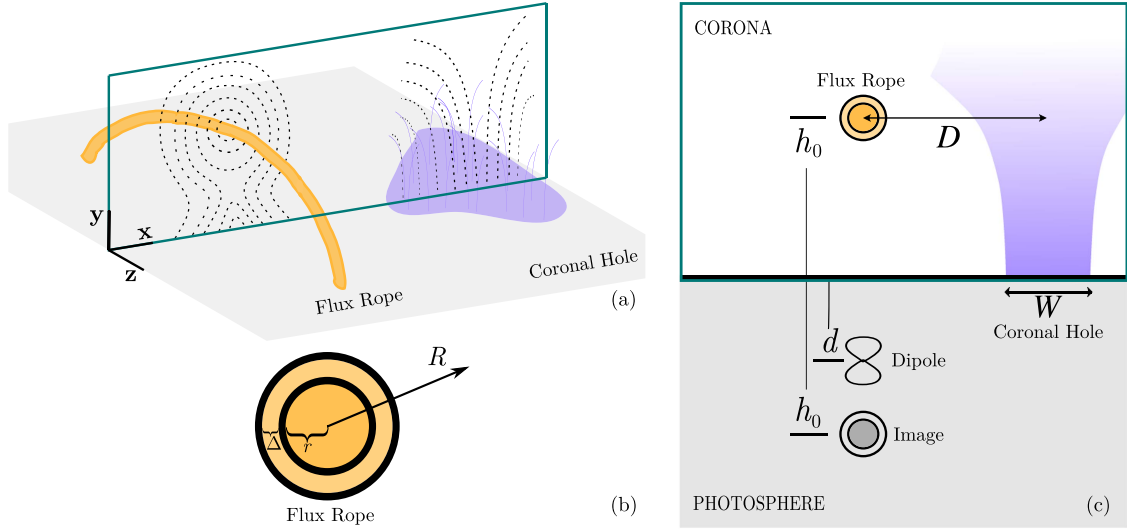
Figure 1. (a) Flux rope and coronal hole scheme. Black dashed lines represent the magnetic field, the orange thick line represents an FR, and the violet region represents a CH. Shaded plane indicates the photospheric surface. (b) Current wire layers: r is the current wire radius, Δ is the thickness of the transition layer between the current wire and the exterior, and R is the radial coordinate from the center of the current wire (in this case, the FR). (c) Components of the magnetic field with their relative two-dimensional positions.

$$j_\phi(R) = j_1 R \left[\sqrt{\left(r - \frac{\Delta}{2}\right)^2 - R^2} \right]^{-1}, \qquad (11)$$

where j_1 is a current density. These expressions are valid inside the flux rope (Z1) and are null in the rest of the domain.

Then, the Cartesian components of the magnetic field in the whole computational domain are given by Mei et al. (2012):

$$
\begin{aligned}
B_x &= -B_\phi(R_-)\frac{(y-h_0)}{R_-} + B_\phi(R_+)\frac{(y+h_0)}{R_+} \\
&\quad - M d B_\phi\left(r + \frac{\Delta}{2}\right)\left(r + \frac{\Delta}{2}\right)\frac{x^2 - (y+d)^2}{R_d^4}, \\
B_y &= B_\phi(R_-)\frac{x}{R_-} - B_\phi(R_+)\frac{x}{R_+} \\
&\quad - M d B_\phi\left(r + \frac{\Delta}{2}\right)\left(r + \frac{\Delta}{2}\right)\frac{2x(y+d)}{R_d^4}, \\
B_z &= B_z(R_-),
\end{aligned}
\qquad (12)
$$

where h_0 is the initial vertical position of the FR and M is the intensity of the line dipole at depth d. The distances R are:

$$
\begin{aligned}
R_\pm &= \sqrt{x^2 + (y \pm h_0)^2}, \\
R_d &= \sqrt{x^2 + (y + d)^2},
\end{aligned}
$$

where R_-, R_+, and R_d are taken from having their origins in the FR, image current wire, and line dipole, respectively. In this way, the first, second, and third terms, for example, of B_x correspond to the x-component of the magnetic field produced by the FR, image current wire and line dipole, respectively. Figure 1(c) shows a scheme with the relative positions between the components of the magnetic field, including the CH.

The temperature inside the FR (T_{FR}) varies according to the following temperature distribution:

$$
T(R_-) = \begin{cases} T_{FR} & \text{at Z1} \\ (T_c - T_{FR})\left[\frac{R_- (r + \Delta/2)}{\Delta}\right] + T_{FR} & \text{at Z2} \\ T_c & \text{at Z3.} \end{cases}
\qquad (13)
$$

The internal pressure of the FR is obtained by proposing a solution close to equilibrium:

$$
\begin{aligned}
p_{FR}(x, y) &= p(y) + \frac{1}{c}\int_R^{r+\frac{\Delta}{2}} B_\phi(R') j_z(R') dR' \\
&\quad - \frac{1}{c}\int_R^{r+\frac{\Delta}{2}} B_z(R') j_\phi(R') dR',
\end{aligned}
\qquad (14)
$$

where $p(y)$ is the background hydrostatic pressure.

We consider that the flux rope length is large enough in order to satisfy the 2.5D assumption, which is in agreement with the observations where lengths of (100–500) Mm are registered (Berger 2014).

2.4. CH Model

The initial magnetic field of the CH is described by (Pascoe et al. 2014):

$$
\begin{aligned}
B_x &= B_0 \sin\left(\frac{x - D}{W}\right) e^{-y/W}, \\
B_y &= B_0 \cos\left(\frac{x - D}{W}\right) e^{-y/W}, \\
B_z &= 0.
\end{aligned}
\qquad (15)
$$

The parameter B_0 is the radial magnetic field strength of the CH at the distance D on the x-axis. The parameter W is related to the width of the CH, and modifies the decay of the strength of magnetic field in the y-direction.

The total initial magnetic field is the sum of the magnetic field of the FR (Equation (12)) and the corresponding CH (Equation (15)). Figure 2 shows the total magnetic field in white lines and the plasma density distribution in the color map. As can be noted, a point of minimum magnetic energy (MME) located at the left of the flux rope ($\sim(-50, 50)$ Mm) is present in this configuration. The FR evolves toward the MME region, as can be seen in the animated version of Figure 2. The relation between the location of the MME region and the CME deflection is analyzed with more detail in Section 3.
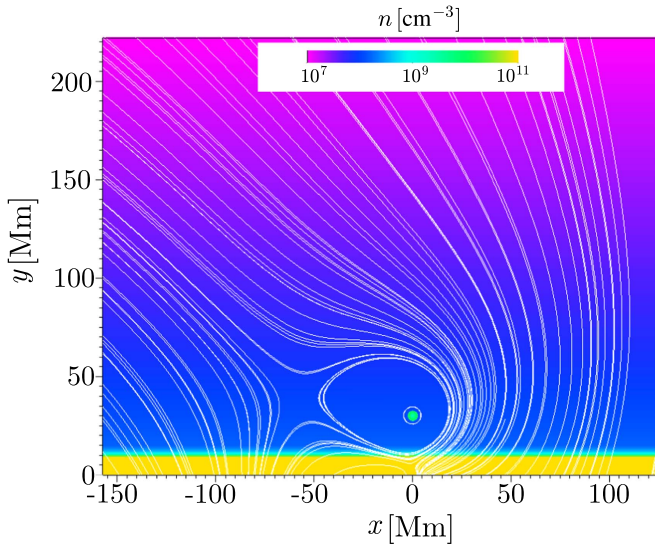
Figure 2. Initial density distribution (color map) and magnetic field lines (white lines). An animated version of this figure, showing the magnetic field lines and density evolution, is available online.

(An animation of this figure is available.)

Table 1
Coronal Holes Parameters for Each Case

Case	B_0 (G)	D (Mm)	W (Mm)
1	0.4	150	400
2	0.8	150	400
3	1.2	150	400
4	1.6	150	400
5	0.8	180	400
6	0.8	250	400
7	0.8	350	400
8	0.8	150	300
9	0.8	150	500
10	0.8	150	600

Table 2
Initial State Parameters

Parameter	Value	
	FR 1	FR 2
j_0 (stA cm^{-2})	435	525
j_1 (stA cm^{-2})	455	300
T_{FR} (MK)	1	4
n_c (cm^{-3})	3×10^8	4.5×10^8
h_0 (Mm)	30	
r (Mm)	2.5	
Δ (Mm)	0.25	
d (Mm)	3.125	
M	1	

Note. Parameters j_0 and j_1 are the current densities inside the flux rope in the z-direction and in the ϕ-direction, respectively, T_{FR} is the internal FR temperature, n_c is the numerical density at the base of the corona, h_0 is the vertical position (height) of the FR, r is its radius, and Δ is the thickness of the transition layer between the FR interior and the corona. Parameters d and M are the depth of the line dipole below the boundary surface and its relative intensity, respectively.

2.5. Parameter Selection

In this study, we simulate warm flux ropes (with temperatures equal to or greater than coronal ones), outside ARs, at a height of 30 Mm with a diameter of 5 Mm (Berger 2014). These FRs usually have extensions of (100–500) Mm; therefore, we consider a characteristic length of $L_0 = 100$ Mm in the z-direction. By the proposed model we obtain number density values inside the FR in the range of $(5 \times 10^8 - 1 \times 10^{10})$ cm^{-3}, which are comparable to the observations reported by Cheng et al. (2012) and Syntelis et al. (2016). To achieve $B \sim 1$ G nearby, for the background magnetic field, we choose the relative intensity and depth of the dipole as were used in Krause et al. (2018).

Our purpose is to analyze how the different characteristics of a CH influence the deflection of coronal mass ejections. To do this, we change the parameters that define the CH and analyze how these changes modify the rising trajectory of the CME. In addition, we want to analyze the dependence of the FR's configuration with regard to the modifications of the CHs. For this, we study the influence of the CH in two different flux ropes (FR1 and FR2) embedded in two different coronal environments, whose number density values at the base of the corona are $n_{c,FR1} = 3 \times 10^8$ cm^{-3} and $n_{c,FR2} = 4.5 \times 10^8$ cm^{-3} (van der Holst et al. 2010; Vásquez 2016). The two simulated FRs have different current densities j_0 and j_1, whose magnetic field values are between $(10 - 100)$ G inside them.

As described in Section 2.4, the parameters of a CH are B_0, D, and W. We choose values to obtain typical nonpolar CH scenarios. Statistical studies found the absolute value of the magnetic field strength to be distributed from 0.2 to 14.0 G, with areas $(A \sim WL_0)$ between $(1.6 \times 10^3 - 1.8 \times 10^5)$ Mm^2 (Hofmeister et al. 2017; Heinemann et al. 2019).

Under these considerations, we perform a parametric study varying the CH features, which is carried out considering the values of Table 1. In Table 2 we show the two configurations of the FR1 and FR2, and the remaining fixed parameters.

3. Results

We quantify the capability of different CH parameters to deviate CME trajectories from the radial direction. We also analyze the relation between the magnetic energy distribution and the CME deflection in order to understand how this deflection is driven by a CH. Given a set of CH parameters, we separately analyze the dynamics of the FR1 and the FR2 configurations.

3.1. Deflection Dependence on CH Parameters

To quantify the deflection we measure the angle formed between the vertical line that passes through the initial position of the FR center, and the line defined by the position of the densest point of the FR and the solar center, as shown in Figure 3. Case 2 (see Table 2) is the reference CH with magnetic field strength $B_{ref} = 0.8$ G and width $W_{ref} = 400$ Mm at a distance of $D_{ref} = 150$ Mm. We simulate the first 600 s (i.e., 10 minutes) of the evolution to analyze the early development of the CME. In order to compare the influence of each parameter on the deflection, we normalize the results with the angle obtained by the FR in case 2, at the final time of the simulation, i.e., $\theta_0 = \theta_{ref}(t = 600$ s$)$. It has to be noted that there are two different reference deflection angles corresponding to each FR1 and FR2 scenario. With these definitions,
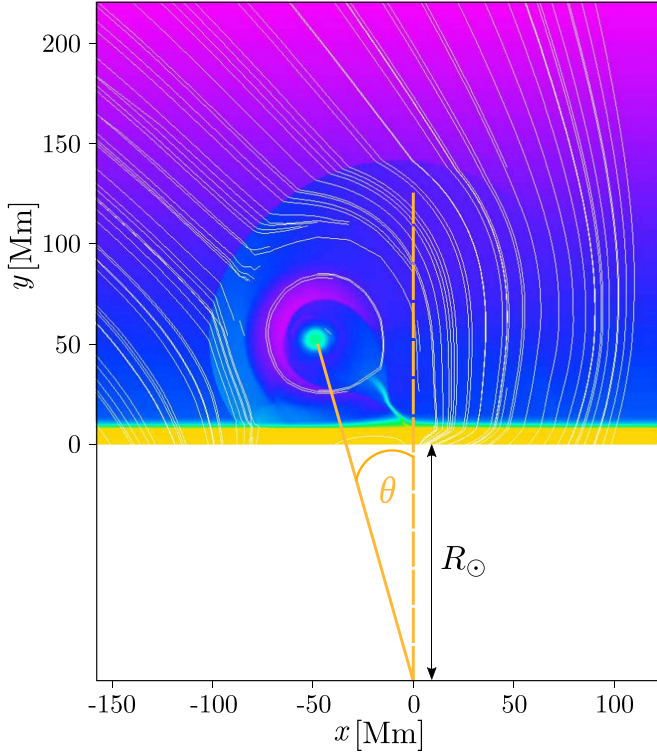
Figure 3. Measurement of the angular deviation of the FR center from the radial direction (deflection angle). The $R_\odot$ is the solar radius. The color scale and white lines are the same as in Figure 2.

we evaluate the relative effect of each CH parameter in the CME evolution, and we compare the results for each FR scenario.

In Figure 4 we show the deviations obtained for FR1 (left panels) and FR2 (right panels) for the different CH configurations. It is noticeable that the influence of the different CHs on both flux rope configurations is similar. All the cases showed a quasi-linear tendency, with a low deceleration, in the deflection angle. The results could be fitted by a quadratic function ($\theta/\theta_0 = at^2 + vt + c$). A more detailed description in terms of the relative deflection velocities v/v_0 (with v_0 the velocity of the reference case) is as follows:

1. The top panels of Figure 4 show the results for cases 1, 2, 3, and 4, for which we simulate CHs of width $W_{\mathrm{ref}} = 400$ Mm at a distance $D_{\mathrm{ref}} = 150$ Mm measured from the flux rope, with different strengths of their magnetic field ($B_0 = [0.4, 0.8, 1.2, 1.6]$ G). The CH of Case 1 ($B_0 = 0.4$ G) triggers a deflection 52% and 49% slower than the reference case (Case 2) for FR1 and FR2, respectively. For Case 3 ($B_0 = 1.2$ G), the CH leads to a deflection velocity 1.3 and 1.15 faster than the reference case for FR1 and FR2, respectively. And, for Case 4 ($B_0 = 1.6$ G), the CH leads to a deflection velocity 1.5 and 1.2 faster than the reference case for FR1 and FR2, respectively.

2. Cases 2, 5, 6, and 7 are shown in the middle panels of Figure 4. These CH configurations have the same magnetic field strength ($B_{\mathrm{ref}} = 0.8$ G) and the same width ($W_{\mathrm{ref}} = 400$ Mm), with different distances from the FR ($D = [150, 180, 250, 350]$ Mm). The CH of Case 5 ($D = 180$ Mm) triggers a deflection that is 4% slower

than the reference case (Case 2), for both FRs. In Case 6 ($D = 250$ Mm) the deflection velocity presents a reduction with respect to the reference case of 15% for FR1 and 14% for FR2. For Case 7 ($D = 350$ Mm) the deflection velocity decreases 36% and 34%, respectively.

3. The bottom panels of Figure 4 show the results of cases 8, 2, 9, and 10, where the simulated CHs have the same magnetic field strength ($B_{\mathrm{ref}} = 0.8$ G) and are located at the same distance from the flux rope ($D_{\mathrm{ref}} = 150$ Mm), with different widths ($W = [300, 400, 500, 600]$ Mm). The results for the CH of Case 8 ($W = 300$ Mm) exhibit a reduction of the deflection velocity of 10% for FR1 and 9% for FR2 in relation to the reference case. For Case 9 ($W = 500$ Mm) the deflection velocity increases by a factor of 1.06 for both FR1 and FR2. Finally, Case 10 ($W = 600$ Mm) shows an increment in the deflection velocity of 1.1, for both FRs.

Following the idea of the "influence parameter" calculated by Gopalswamy et al. (2009), where $f \sim B_0 A/D^2$, and given the quasi-linear trend of the relative deflection velocities v/v_0 described above, we analyze this dimensionless quantity (named $\mathfrak{f}$ hereafter) as a function of B_0, W, and D^{-2}. Figure 5 shows the linear fit (orange filled line) and its standard deviation (orange shadow area) obtained for the different CHs parameters. The top, middle, and bottom panels show the fits:

$$\mathfrak{f}_B = \alpha_B W_{\mathrm{ref}} D_{\mathrm{ref}}^{-2} B_0,$$
$$\mathfrak{f}_D = \alpha_D W_{\mathrm{ref}} B_{\mathrm{ref}} D^{-2},$$
$$\mathfrak{f}_W = \alpha_W B_{\mathrm{ref}} D_{\mathrm{ref}}^{-2} W,$$

taking into account the results of both FRs. The green square and magenta diamond symbols represent the values of v/v_0 obtained from FR1 and FR2, respectively. From these fits we obtained $\alpha_B = (48 \pm 8)$, $\alpha_D = (31 \pm 7)$, and $\alpha_W = (18 \pm 3)$ in units of (Mm G^{-1}). With black dotted line we show the average $\bar{\mathfrak{f}} = \bar{\alpha}\frac{BW}{D^2}$, where $\bar{\alpha} = (32 \pm 4)$ (Mm G^{-1}) is the average of α_i, with the $i = B_0, D, W$. This dimensionless parameter average is in agreement with the fit values obtained for the magnetic field strength and the inverse square of the distance, but overestimates the relative deflection velocities obtained for the variation of the width ($\bar{\alpha} > \alpha_W$).

3.2. Deflection Dependence on the MME Position

Previous works mention that CHs can act as magnetic walls that avoid the radial evolution of CMEs (Gopalswamy et al. 2009). However, it is not clear the physical mechanisms involved in this process. As shown in Section 2.4, the CH generates a region of MME located to the left of the FR. To understand the role of this null point in the CME deflection, in Figure 6 we plot the FR path for each case, up to $t = 600$ s, overlapped to the position of the corresponding minimum of magnetic energy, at the initial time ("x" marks in the plots).

We can see again that even though both flux ropes follow different paths, they have a similar behavior under the variation of CH parameters. Below we analyze each case path according to the variation of the parameters used:

1. The top panels of Figure 6 show the paths for cases 1, 2, 3, and 4, where the magnetic field strength is varied
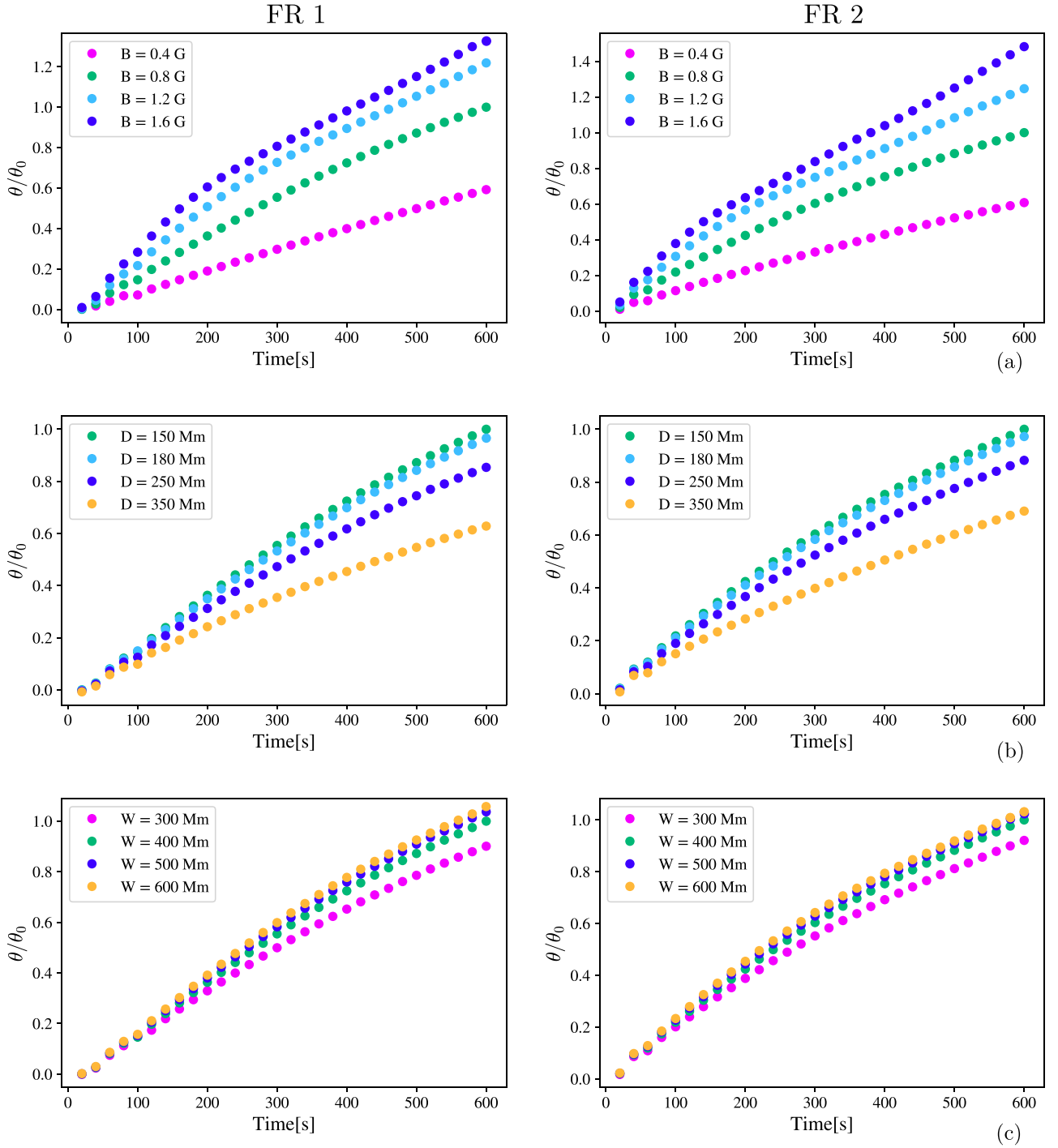
Figure 4. Angular deviation of the FR center from the vertical direction (deflection), as a function of time for different (a) magnetic field strengths, (b) distances, and (c) widths of CH.

$(B_0 = [0.4, 0.8, 1.2, 1.6]$ G). As can be seen, the stronger the magnetic field, the closer the position of the MME to the FR. This produces a strong difference in the early stages of the FR evolution and in their velocities. For the later evolution all cases seem to be channeled in the same path. It must be noted that the CHs of these cases have field lines of the same shape, as discussed below.

2. Cases 2, 5, 6, and 7 are shown in the middle panels of Figure 6. These CH configurations have different

distances from the FR ($D = [150, 180, 250, 350]$ Mm). For these cases we can see that the closer the CH to the FR, the closer the position of the MME to the FR too. In addition, it appears that the lower (in y-direction) the position of the MME region, the slower the rising of the flux rope.

3. The bottom panels of Figure 6 show the paths of cases 8, 2, 9, and 10, where the simulated CHs have different widths ($W = [300, 400, 500, 600]$ Mm). The wider the CH, the closer the position of the MME to the FR. For
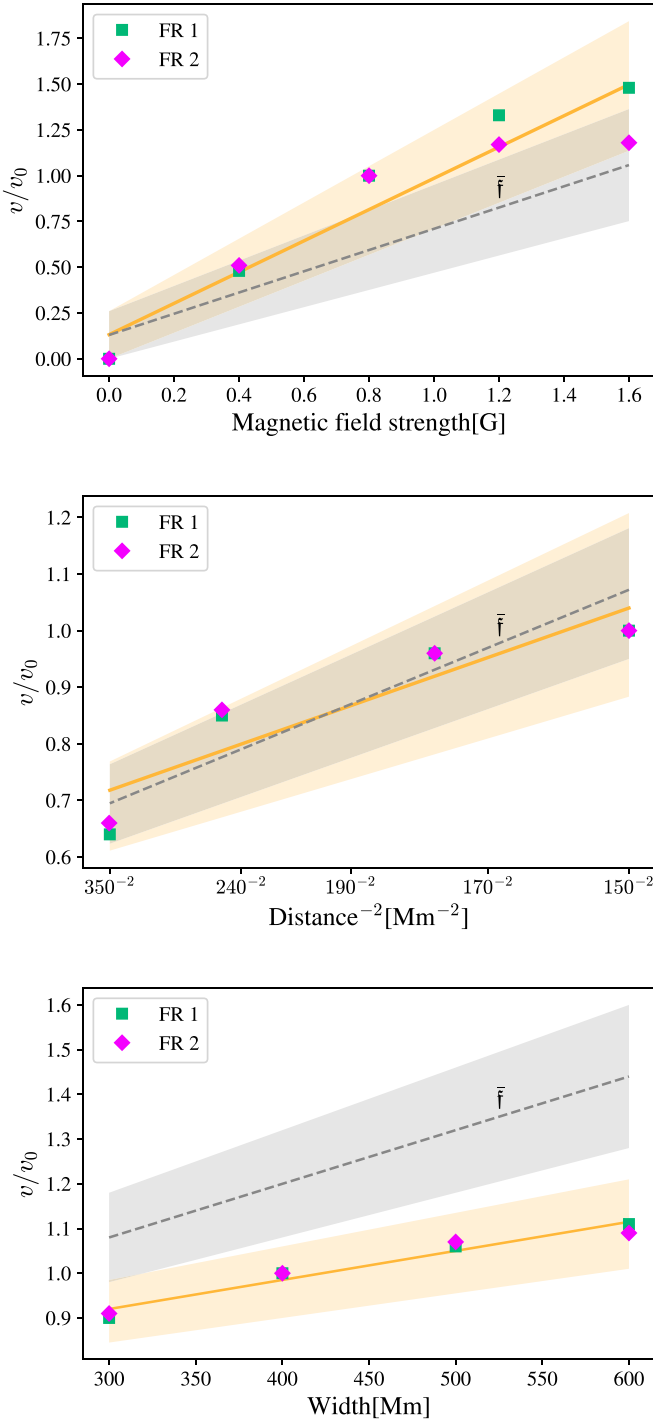
Figure 5. Linear fit for the CH parameters (orange line) with their standard deviation (orange shadow area). The black dashed line represents the dimensionless parameter average with its standard deviation (gray shadow area).

these cases, as in the previous item, the lower (in *y*-direction) the position of the MME region, the slower rising of the flux rope.

For this qualitative analysis we note that the distance from the point of minimum magnetic energy to the flux rope (measured at $t = 0$ s) seems to play an important role, mainly in the first stage of the evolution.

In order to evaluate the relation between the position of the MME region and the CME deflection, we compare the relative change in the initial distance between the MME point and the FR with respect to the reference case, i.e., $(d_0 - d)/d_0$ (%), and the corresponding relative change in the deflection velocities $(v - v_0)/v_0$ (%). In other words, we want to know how much closer the MME point is to the FR for a given change of the deflection velocity. In the top panel of Figure 7 we plot the relative changes of the initial MME distances and the deflection velocities for different magnetic field strengths. Note the trend by which the stronger the magnetic field, the closer the MME point to the FR and the larger the deflection. Still, the change in the deflection velocity can be larger or smaller than the change in the MME distance, depending on the FR configuration. In addition, weak magnetic fields are directly related to the relative change in the MME distance and the relative variation of the deflection velocity. We now consider the effect of the distance of the flux rope to the CH, we plot the middle panel of Figure 7, where a similar trend as in the previous case is observed: the closer the distance to the CH, the closer the MME region to the FR and the larger the deflection. We can see that the relative changes of the deflection velocities are larger than the relative variation of the MME distance, for both FR configurations. The influence of the CH width is presented in the bottom panel of Figure 7. We see again a similar trend, implying that the wider the CH, the closer the MME point to the FR and the larger the deflection. Contrarily to the results of the CH distance analysis, in this case, the relative change in the MME distance is larger than the relative variation of the deflection velocity.

Considering the previous analysis, we conclude that the closer the MME region position to the FR, the larger the deflection of the CME. However, their relation seems to be complex and dependent on other parameters of the problem. That is, different configurations with equal initial distance between the MME point and the FR center will not necessarily exhibit similar deflections due to the probable action of other parameters affecting the CME trajectory, as shown in Figure 8.

In reference to the physical mechanisms involved in the CME deflections due to the CH presences we identify the following aspects. First, we note that the MME point produced by the overlapping of the different magnetic structures is initially an attracting point of the flux rope, whose effect is significant at the early stages of the evolution. The reason why the FR does not reach the MME point is because the minimum of magnetic energy is dispersed when the bow shock generated by the rising FR impacts the minimum energy location. Therefore, although the FR is initially attracted by the MME region, it is deflected by another factor when the region is stretched and dragged by the shock. Based on the results shown in the first panel of Figure 6, we suggest that the second mechanism that triggers the deflection is the channeling of the FR, which is evident in Figure 8. This channel is defined by the CH magnetic field lines, combined with the background magnetic field. From our simulations, we infer that a CH acts as a magnetic wall, which can have a remote repulsive action, through the formation of an MME and a channel that triggers the deflection of the flux rope.

4. Conclusions and Discussion

The study of CME deflections is of great interest to the space weather forecast. Many efforts have been carried out to understand how the intrinsic properties of the CME or the
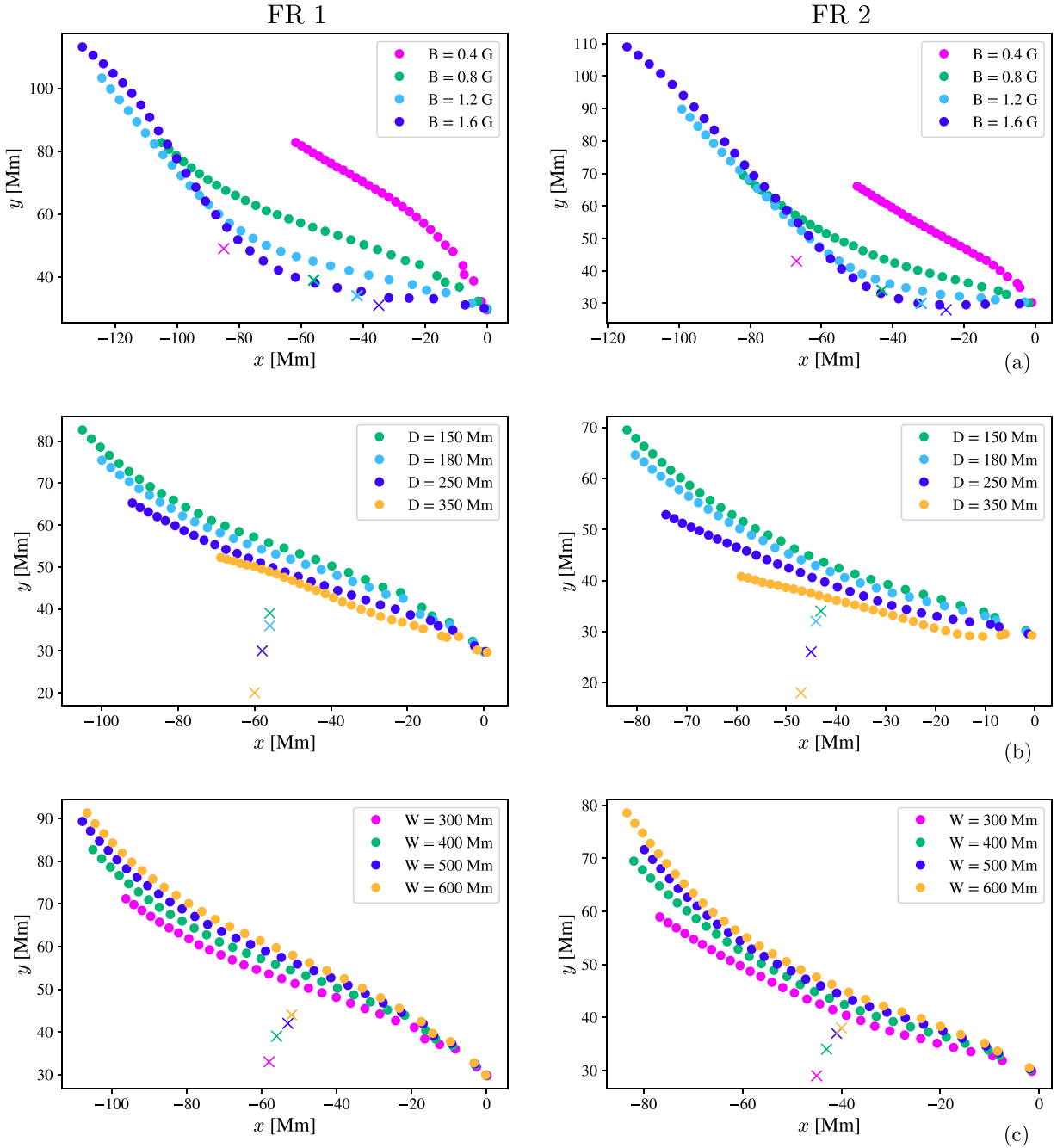
Figure 6. Path of the FR center (dots) up to $t = 600$ s, and the position of the MME at $t = 0$ s (x), for different (a) magnetic field strengths, (b) distances, and (c) widths of the CH.

magnetic structures of the environment can influence the deflections. Some of the most studied coronal magnetic structures are the CHs. To quantify the influence of CHs on the CME deflections, several authors use an influence parameter, which depends on the intrinsic features of the CHs (Cremades et al. 2006; Gopalswamy et al. 2009; Mohamed et al. 2012). In our analysis of the early stages of a CME deflection in the presence of a CH, we obtained that the deflection increases for wider CHs, with stronger magnetic fields, and decreases when the CH moves away from the flux rope. Also, we found similar behaviors for two different FRs, which suggest that the influence of the parameters of the CH is mostly independent of the FRs scenarios.

From the complete set of simulations, a tendency is revealed: the deviation angle grows almost linearly with a low deceleration. This deceleration could be attributed to the increasing distance between the CH and the CME as it rises, consequently reducing the CH influence in the CME trajectory. Moreover, we found a dimensionless parameter related with the velocity of the deflection that behaves similarly to the influence parameter proposed by Gopalswamy et al. (2009). We obtained that the relative deflection velocity increases linearly with the magnetic field strength and decreases with the inverse square of the distance. However, the relative deflection velocities, obtained from the width variations, are lower than the values obtained from the proposed linear behavior. It is worth
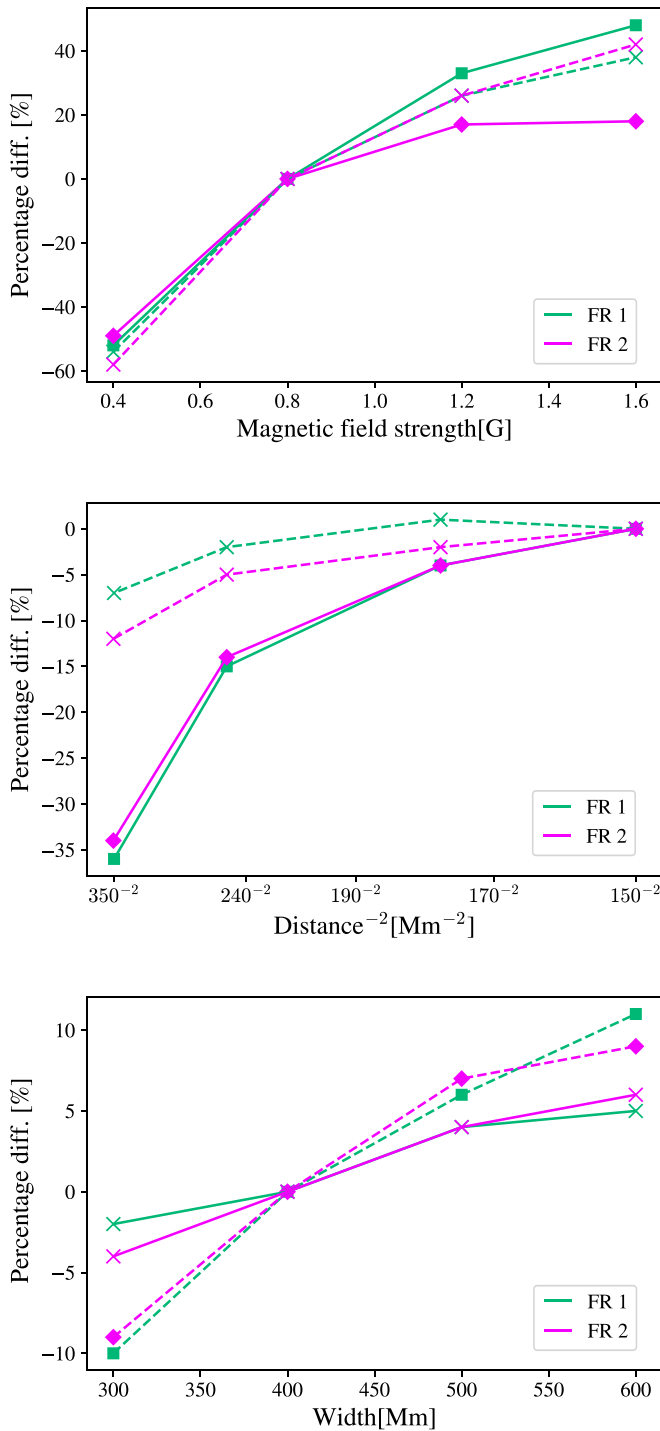
Figure 8. Path of the FR center (dots), and the position of the MME at $t = 0$ s (x), for different FRs and different magnetic field strengths of CH. The color map represents the magnetic energy density and the black lines represent the magnetic field lines.

point of MME and the FR; this relationship shows that both quantities depend on the parameters of the CH. For the later evolution of the ejection, we notice a channeling of the flux rope. We proposed that the formation of the MME point and the channel that lead to the deflection of the FR, are a consequence of the presence of the CH, attributing to it the remote action of a magnetic wall.

To conclude, we reinforce the fact that the presence of CHs in the area of the CME formation is of crucial importance in the later evolution of the event. This systematic study of the influence of the CH properties in the CME early evolution can help to characterize the effect of these magnetic structures in the full evolution of coronal mass ejections.

ORCID iDs

Mariana Cécere ⓘ https://orcid.org/0000-0002-9844-0033

Figure 7. Percentage of $(d_0 - d)/d_0$ (%) (dashed lines) and percentage of $(v - v_0)/v_0$ (%) (solid lines) in functions of the CH parameters.

mentioning that such overestimation could be explained either by the inaccuracy of the proposed model as well as by an inaccurate definition of the CH width. The mathematical width used could be overestimating the effective size of the CH.

We found some interesting physical insights related with the CH influence on CME deviations. We showed that an MME point is produced by the overlapping of different magnetic structures, which changes the trajectory of the flux rope, mainly in its early evolution. There is a relationship between the speed of deviation of the CME and the initial distance between the
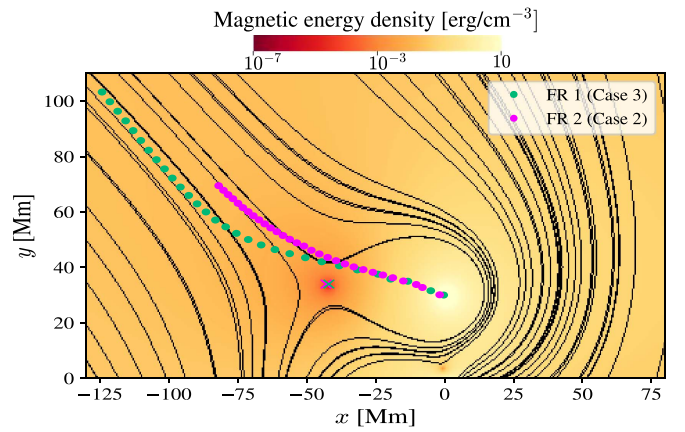
References

Berger, T. 2014, in IAU Symp. 300, Nature of Prominences and their Role in Space Weather, ed. B. Schmieder, J.-M. Malherbe, & S. T. Wu (Cambridge: Cambridge Univ. Press), 15
Capannolo, L., Opher, M., Kay, C., & Land, I. E. 2017, ApJ, 839, 37
Cécere, M., Sieyra, M., Cremades, H., et al. 2019, AdSpR, 65, 1654
Cheng, X., Zhang, J., Saar, S. H., & Ding, M. D. 2012, ApJ, 761, 62
Cremades, H., Bothmer, V., & Tripathi, D. 2006, AdSpR, 38, 461
Forbes, T. G. 1990, JGR, 95, 11919
Fryxell, B., Olson, K., Ricker, P., et al. 2000, ApJS, 131, 273
Gopalswamy, N., Mäkelä, P., Xie, H., Akiyama, S., & Yashiro, S. 2009, JGRA, 114, A00A22
Heinemann, S. G., Temmer, M., Heinemann, N., et al. 2019, SoPh, 294, 144
Hofmeister, S. J., Veronig, A., Reiss, M. A., et al. 2017, ApJ, 835, 268
Jin, M., Manchester, W. B., van der Holst, B., et al. 2017, ApJ, 834, 172

Kay, C., Opher, M., & Evans, R. M. 2013, ApJ, 775, 5

Kay, C., Opher, M., & Evans, R. M. 2015, ApJ, 805, 168

Kilpua, E. K. J., Pomoell, J., Vourlidas, A., et al. 2009, AnGeo, 27, 4491

Krause, G. 2019, A&A, 631, A68

Krause, G., Cécere, M., Zurbriggen, E., et al. 2018, MNRAS, 474, 770

Landi, E., Raymond, J. C., Miralles, M. P., & Hara, H. 2010, ApJ, 711, 75

Lee, D., & Deane, A. E. 2009, JCoPh, 228, 952

Liewer, P., Panasenco, O., Vourlidas, A., & Colaninno, R. 2015, SoPh, 290, 3343

Lugaz, N., Downs, C., Shibata, K., et al. 2011, ApJ, 738, 127

Lynch, B. J., & Edmondson, J. K. 2013, ApJ, 764, 87

Mäkelä, P., Gopalswamy, N., Xie, H., et al. 2013, SoPh, 284, 59

Mei, Z., Shen, C., Wu, N., et al. 2012, MNRAS, 425, 2824

Mohamed, A. A., Gopalswamy, N., Yashiro, S., et al. 2012, JGRA, 117, A01103

Möstl, C., Rollett, T., Frahm, R. A., et al. 2015, NatCo, 6, 7135

Panasenco, O., Martin, S., Joshi, A. D., & Srivastava, N. 2011, JASTP, 73, 1129

Panasenco, O., Martin, S. F., Velli, M., & Vourlidas, A. 2013, SoPh, 287, 391

Pascoe, D. J., Nakariakov, V. M., & Kupriyanova, E. G. 2014, A&A, 568, A20

Robertson, J. A., & Priest, E. R. 1987, SoPh, 114, 311

Syntelis, P., Gontikakis, C., Patsourakos, S., & Tsinganos, K. 2016, A&A, 588, A16

van der Holst, B., Manchester., W. B. I., Frazin, R. A., et al. 2010, ApJ, 725, 1373

van Tend, W., & Kuperus, M. 1978, SoPh, 59, 115

Vásquez, A. M. 2016, AdSpR, 57, 1286

Wang, J., Hoeksema, J. T., & Liu, S. 2019, arXiv:1909.06410

Xie, H., St., Cyr, O. C., Gopalswamy, N., et al. 2009, SoPh, 259, 143

Yang, J., Dai, J., Chen, H., Li, H., & Jiang, Y. 2018, ApJ, 862, 86

Zhou, Y., Feng, X., & Zhao, X. 2014, JGRA, 119, 9321

Zhou, Y. F., & Feng, X. S. 2013, JGRA, 118, 6007

Zhuang, B., Wang, Y., Shen, C., et al. 2017, ApJ, 845, 117

Zuccarello, F. P., Bemporad, A., Jacobs, C., et al. 2012, ApJ, 744, 66